Title

X-ray free electron laser linear accelerator without a laser heater

Author
Qiang, Ji

Publication Date
2023-03-01

DOI
10.1016/j.nima.2022.167968

X-ray free electron laser linear accelerator without a laser heater

Ji Qiang

Lawrence Berkeley National Laboratory, Berkeley, CA 94720

Abstract

Linear accelerator based X-ray free electron laser (FEL) light sources provide an important tool for scientific discoveries. Most of these light source facilities employ a laser heater to increase the electron beam's uncorrelated energy spread to suppress microbunching instability through the linear accelerators. In this paper, we first studied the microbunching instability in an x-ray FEL linear accelerator with lower initial peak current (~ 10 A) and moderate final peak currents ($1-2$ kA). In this regime, the microbunching instability can be substantially mitigated with modest initial uncorrelated energy spread. We then suggested a less expensive method to mitigate the microbunching instability using a section of low beta FODO lattice instead of the laser heater. With the use of the high brightness electron beam from a photoinjector, the intrabeam scattering effect inside the beam through the FODO lattice can generate sufficient uncorrelated energy spread to mitigate the microbunching instability. At last, we demonstrated the feasibility of this method with self-consistent solution of the Fokker-Planck equation through the x-ray FEL linear accelerator.

1. Introduction

The coherent x-ray radiation from an x-ray free electron laser (FEL) light source provides an important tool for scientific discoveries in physics, chemistry, biology and other fields. To produce such a radiation at short x-ray wavelength effectively, it is desirable to use a high brightness electron beam with a high peak core current, small energy spread, and small emittance produced from a linear accelerator with a single or multiple stage compressions. However, the microbunching instability starting from the shot-noise in the electron beam and driven by collective effects can result in large longitudinal phase space filamentation and reduce the electron beam brightness [1, 2, 3, 4, 5, 6, 7, 8, 9, 10, 11, 12]. In order to mitigate the instability, extra uncorrelated energy spread is introduced at the beginning of the linear accelerator by using a device called laser heater [13, 14]. This device uses a laser beam interacting with the electron beam inside a short undulator located between the second and the third bending magnets of a chicane. The electron beam passing through the laser heater chicane attains extra uncorrelated energy spread from the laser induced energy modulation. Such a device provides an effective control of the electron beam uncorrelated energy spread and was widely adopted in most modern linear accelerator based x-ray FEL light sources [15, 16, 17, 18, 19] even though several different but less mature methods were proposed to mitigate the microbunching instability [20, 21, 22, 23, 24, 25].

On the other hand, the use of a laser heater increases the cost of accelerator construction and operation. In this paper, we first studied the microbunching instability inside an x-ray FEL linear accelerator under a different regime from the present x-ray FEL accelerators. This linear accelerator employs an electron beam with a lower initial peak current ($\sim$ 10 A) from a high repetition rate (MHz) photoinjector. The final peak current at the exit of the accelerator will be between one and two kilo-Amperes passing through two bunch compressors inside the accelerator. The example of this type of x-ray FEL accelerator includes LCLS-II and SHINE that are under construction [26, 27, 28]. For such an accelerator, we estimated the microbunching instability gain through the accelerator and observed that modest initial uncorrelated energy spread is needed to substantially mitigate the microbunching gain. Next, we suggested an alternative, less expensive method based on a section of low beta FODO lattice to introduce extra uncorrelated energy spread through the intrabeam scattering effect. This idea was considered in reference [29] but was rejected in that reference with the conclusion of insufficient uncorrelated energy spread from the intrabeam scattering effect through the lattice. Instead, a ring was proposed to attain sufficient uncorrelated energy spread. For the type of x-ray FEL linear accelerator in the new regime, we revisited this idea using an initial lower peak current high brightness electron generated from a low emittance ($\sim$ 0.1 mm mrad)injector. Such low emittance injectors have been actively pursued in a number of studies [30, 31, 32, 33]. For the low emittance beam, one can take advantage of the intrabeam scattering effect through the low beta FODO lattice to attain sufficient uncorrelated energy spread to mitigate the microbunching instability. In order to demonstrate the feasibility of this method, we simulated an electron beam transport through the accelerator including the intrabeam scattering effect by solving the Fokker-Planck equation self-consistently.

The organization of this paper is as follows: after the Introduction, we give an analytical calculation of the microbunching instability gains through a double compressor x-ray FEL linear accelerator with an initial lower current in Section II; estimate the uncorrelated energy spread induced through a low beta FODO lattice in Section III, demonstrate the feasibility in an application example with the self-consistent simulation of a low emittance electron beam through the low beta FODO lattice and the linear accelerator in Section IV, and draw conclusions in Section V.

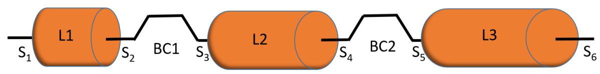

Figure 1: Schematic plot of an x-ray FEL linear accelerator with two bunch compressors.

2. Microbunching instability through a linear accelerator

In an x-ray FEL linear accelerator, a small initial current modulation in the electron beam (even from shot noise) can be amplified through the accelerator. This phenomenon is usually called microbunching instability. The initial current modulation induces energy modulation due to collective effects such as the space-charge effect. The energy modulation is further amplified by the collective effects along the linear accelerator. After a bunch compressor, the amplified energy modulation becomes larger current modulation and amplifies the initial current modulation. The microbunching instability can cause large final beam phase space filamentation and degradation of the electron beam quality.

In the x-ray FEL linear accelerator with two-stage compression as shown in Fig. 1, the microbunching instability amplification gain factor through the accelerator can be calculated using an analytical model [3, 4]. This model showed reasonable agreement with the experimental measurement [11] and the self-consistent macroparticle simulation [25]. Such an analytical model helps decide on the level of initial uncorrelated energy spread needed to mitigate the microbunching instability. Assuming an electron beam with an initial current modulation factor b_0 at the entrance (s_1) to L1, the modulation factor at a location s of the accelerator can be obtained by solving the following integral equation:

$$b[k(s); s] \quad = \quad b_0[k(s); s] + \int_{s_1}^{s} K(\tau, s) b[k(\tau); \tau] d\tau \tag{1}$$

where $b_0[k(s); s]$ denotes the initial modulation factor evolution without subject to the collective effects. The kernel of the above integral equation is given as:

$$K(\tau; s) = ik(s)\hat{R}_{56}(\tau \to s)\frac{I(\tau)}{I_A}\frac{Z[k(\tau);\tau]}{\gamma_0}\exp\big(-\frac{k_0^2}{2}U^2\sigma_{\delta 0}^2\big) \quad (2)$$

where $U(s,\tau) = C(s)R_{56}(s) - C(\tau)R_{56}(\tau)$ and the Alfvén current $I_A \simeq 17.045$ kA.

The above integral equation can be solved iteratively. Assuming that electron beam is longitudinally frozen inside the three linac sections (L1, L2, and L3) and neglecting the collective effects inside the two bunch compressors (BC1 and BC2), we can obtain the final modulation factor at the exit of L3 (s_6) as:

$$b[k(s_6); s_6] = b_{06}[k(s_6); s_6] + b_{12}[k(s_6); s_6] + b_{34}[k(s_6); s_6] + b_{1234}[k(s_6); s_6] \quad (3)$$

where $k(s) = C(s)k_0$ and $C(s)$ is the compression factor from s_1 to s, and k_0 is the initial modulation wave number. Here b_{06} denotes evolution of the modulation factor in the absence of any collective effects, and is given as:

$$b_{06}[k(s_6); s_6] = b_0 \exp(-\frac{k^2(s_6)\hat{R}_{56}^2(s_{1\to 6})\sigma_{\delta_0}^2}{2}) \quad (4)$$

where b_0 denotes the initial modulation factor at location s_1. The terms of b_{12} and b_{34} denote amplification of the initial modulation due to the collective effects between the linac section of $s_{1\to 2}, s_{3\to 4}$ respectively, and are given as:

$$b_{12}[k(s_6); s_6] = ib_0 k(s_6)\hat{R}_{56}(s_{1\to 6})\frac{I(s_1)}{\gamma_0}\hat{Z}(s_{1\to 2})\exp(-\frac{k_0^2\mathcal{D}^2(s_{1\to 6})\sigma_{\delta_0}^2}{2}) \quad (5)$$

$$b_{34}[k(s_6); s_6] = ib_0 k(s_6)\hat{R}_{56}(s_{3\to 6})\frac{I(s_3)}{\gamma_0}\hat{Z}(s_{3\to 4})\exp(-\frac{k_0^2\mathcal{D}^2(s_{3\to 6})\sigma_{\delta_0}^2}{2}) \quad (6)$$

The b_{1234} term denotes the two-section coupling effect between the section $s_{1\to 2}$

and $s_{3\to4}$ and is given as:

$$b_{1234}[k(s_6);s_6] = -b_0 k(s_3)k(s_6)\hat{R}_{56}(s_{1\to3})\hat{R}_{56}(s_{3\to6})\frac{I(s_1)I(s_3)}{(\gamma_0)^2}\hat{Z}(s_{1\to2})\hat{Z}(s_{3\to4}) \times \exp\left(-\frac{k_0^2\mathcal{D}^2(s_{1\to3\to6})\sigma_{\delta_0}^2}{2}\right) \quad (7)$$

where σ_{δ_0} is the initial RMS relative uncorrelated energy spread, γ_0 is the initial electron beam relativistic factor, $I(s_j) = C(s_j)I_0$, and I_0 is the initial current. The impedance $\hat{Z}$ in the above equations is defined as:

$$\hat{Z}(s_{j\to k}) = \int_{s_j}^{s_k} \frac{4\pi Z[k(\tau);\tau]}{I_A Z_0} d\tau,$$

where $Z[k(\tau);\tau]$ is the impedance per unit length and Z_0 is the vacuum impedance. The exponential damping to modulation amplification due to the initial energy spread is given as:

$$\mathcal{D}^2(s_{1\to6}) = U^2(s_6, s_1) \quad (8)$$

$$\mathcal{D}^2(s_{3\to6}) = U^2(s_6, s_3) + U^2(s_3, s_1) \quad (9)$$

$$\mathcal{D}^2(s_{1\to3\to6}) = U^2(s_6, s_3) + U^2(s_3, s_1) \quad (10)$$

where $U(s,\tau) = C(s)\hat{R}_{56}(s) - C(\tau)\hat{R}_{56}(\tau)$, $\hat{R}(s) = \hat{R}(s_1 \to s)$, and

$$\hat{R}_{56}(s_{1\to3}) = \tfrac{R_{56,1}\gamma_1}{\gamma_3} \quad (11)$$

$$\hat{R}_{56}(s_{1\to6}) = \tfrac{R_{56,1}\gamma_1}{C_2\gamma_3} + \tfrac{R_{56,2}C_1\gamma_1}{\gamma_5} \quad (12)$$

$$\hat{R}_{56}(s_{3\to6}) = \tfrac{R_{56,2}\gamma_1}{\gamma_5} \quad (13)$$

In the above equations, we have assumed the space-charge effect as the only collective effect inside three linac sections and neglected the collective effects inside BC1 and BC2 since the space-charge effect is the dominant factor contributing to microbunching instability [34, 35]. The longitudinal space-charge impedance for round uniform electron beam is given as [36]:

$$Z(k,s) = \frac{iZ_0}{\pi\gamma r_b}\frac{1-2I_1(\zeta)K_1(\zeta)}{\zeta}|_{\zeta=kr_b/\gamma} \tag{14}$$

where r_b is the beam radius, k is the wave number, γ is the relativistic factor, and I_1, K_1 are modified Bessel functions of the first kind. The momentum compaction factors (R_{56}) inside $L1$, $L2$, and $L3$ are set to zero from the longitudinally frozen beam assumption.

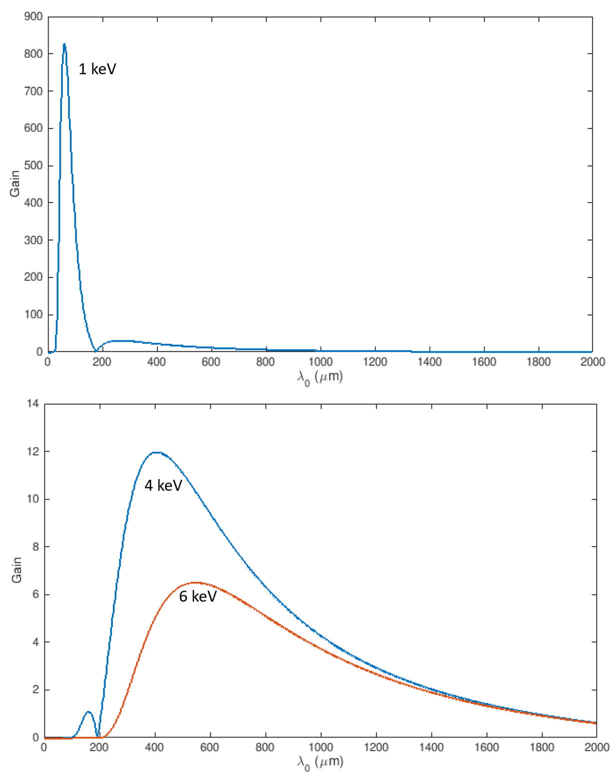

Figure 2: Microbunching gain as a function of initial modulation wavelength with 1 keV initial uncorrelated energy (left), 4 keV and 6 keV initial uncorrelated energy spread (right).

From the above equations we see that the gain of the microbunching instability depends strongly on the electron beam initial uncorrelated energy spread.

For the x-ray FEL linear accelerator in Fig. 1, with an electron beam from a low emittance injector, we calculated the microbunching instability gain as a function of initial modulation wavelength for several initial uncorrelated energy spreads in Fig. 2. Here, we have used an initial low emittance electron beam with 0.1 mm mrad normalized transverse emittance and 10 Ampere current. The electron beam energy is 100.0 MeV at s_1, 200.0 MeV at s_3, 1600.0 MeV at s_5, and about 8.0 GeV at s_6. The momentum compaction factor of bunch compressor BC1 is 4.0 cm, and of BC2 is 5.3 cm. The compression factors are 3.6 through BC1 and 42.0 through BC2. At the beginning of the linac L1, we assumed a section of 36 meter FODO lattice. The electron beam average transverse RMS size inside this section is 16.0 microns. Following this lattice, the electron beam is accelerated linearly through a section of 50 meter superconducting cavities before BC1. The average transverse RMS size in this section is about 150.0 microns. After the BC1, we assumed that the electron beam is linearly accelerated through the linac L2 with a length of 200 meters before entering BC2. The average transverse RMS size is assumed to be 75.0 microns. After the BC2, the electron beam is further accelerated and transported to the end of the linac L3. From the above figure, it is seen that with a small initial uncorrelated energy spread (1 keV), the microbunching instability gain will be more than 800. However, with an initial 6 keV uncorrelated energy, the instability gain is substantially reduced and drops below 10. Such an amount of uncorrelated energy spread can be generated by the intrabeam scattering effect inside a low emittance electron beam through a low beta FODO lattice.

The microbunching instability gain increases with the increase of the initial current. Figure 3 shows the calculated gain as a function of initial modulation wavelength at the exit of the above linear accelerator with an initial 10 A, 20 A, and 40 A peak currents, 6 keV uncorrelated energy spread, and the same

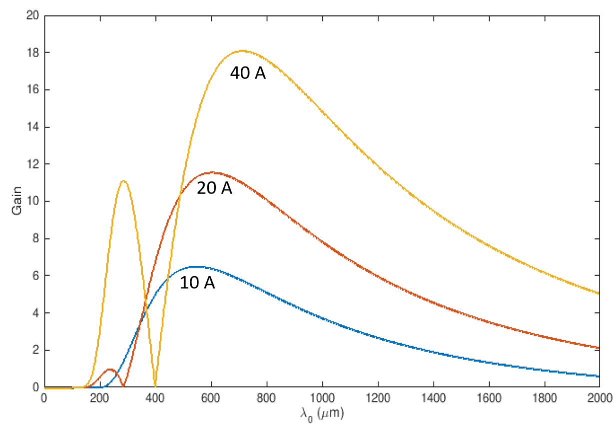

Figure 3: Microbunching gain as a function of initial modulation wavelength with initial 10 A, 20 A, and 40 A peak current and 6 keV uncorrelated energy spread.

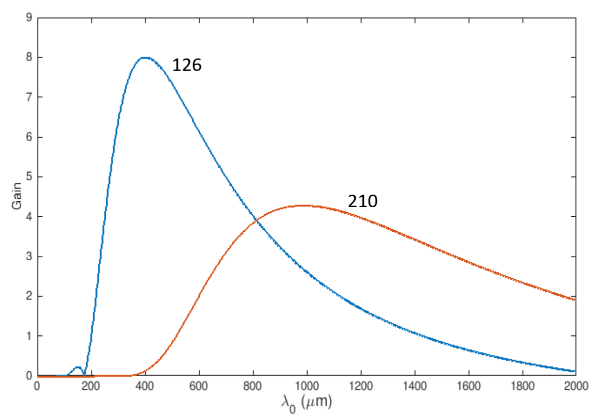

Figure 4: Microbunching gain as a function of initial modulation wavelength with 126 and 210 total compression factor and initial 10 A current and 6 keV beam.

overall compression factor. The maximum gain reaches near 20 for the 40 A initial current. A smaller gain peak at a shorter modulation wavelength is seen for this initial current.

The microbunching instability gain also depends on the total compression factor through the accelerator. With a fixed compression factor through bunch compressor two (BC2), we adjusted the compression factor through BC1 to a factor of 3 and 5 with an initial 10 A peak current and 6 keV uncorrelated energy spread electron beam. Figure 4 shows the instability gain as a function of initial modulation wavelength with these two compression factors. It is seen that smaller compression factor results in larger maximum gain towards shorter wavelength. This is due to exponential dependency of the gain on the compression factor and wavelength in the analytical model. Lower initial peak current and higher compression might produce even lower microbunching gain. On the other hand, higher compression might induce more nonlinear effects through the bunch compressors and distort the longitudinal current profile. The choice of the working point in the accelerator is based on the balance of multiple factors.

The above model assumes a flat electron beam current. For a real beam with a current distribution along the bunch length, the microbunching gain can be different along the bunch. If the flat current used in the analytical model is chosen close to the maximum value of the real current distribution, it would yield an upper bound of the microbunching gain for the real beam.

3. Uncorrelated energy spread due to intrabeam scattering inside a FODO lattice

The intrabeam scattering effect due to multiple small-angle Coulomb collisions inside a charged particle beam can have significant impact on beam lifetime in circular accelerators. For a high-brightness electron beam inside an x-ray FEL linear accelerator, this effect can increase the energy spread of the electron beam through the accelerator while has negligible effect on transverse emittances since the electron beam is much colder in the longitudinal direction than in transverse ones [37, 38, 39, 40]. The resultant RMS uncorrelated energy spread σ_γ as a function of distance s in the linear accelerator is given as [37]:

$$\sigma_\gamma^2 = \sigma_{\gamma 0}^2 + \frac{r_e^2 N_b \ln \Lambda}{4 < \sigma_x > \epsilon_x^n \sigma_z} s \qquad (15)$$

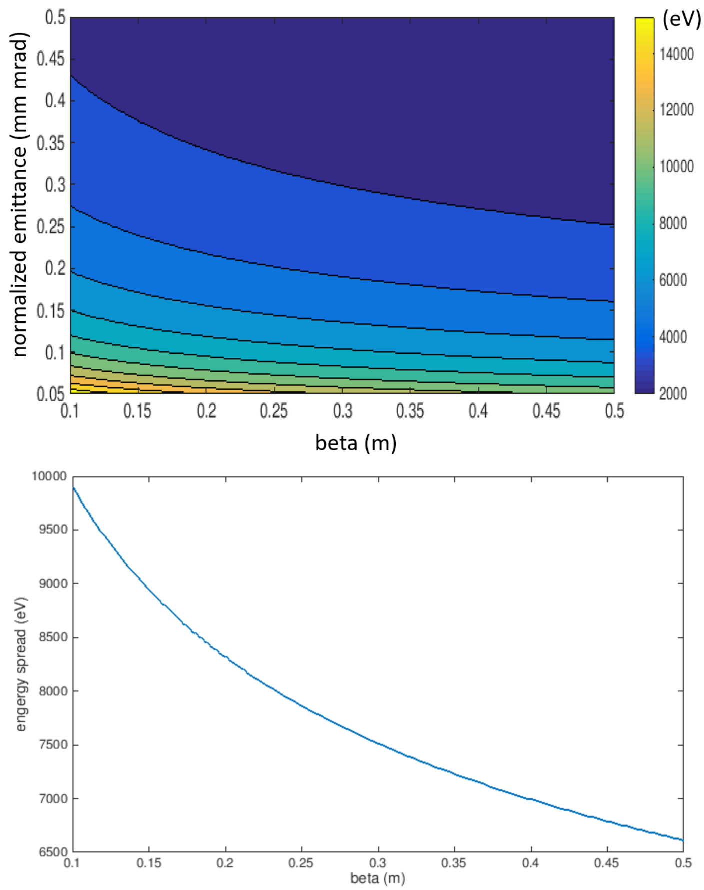

Figure 5: Uncorrelated energy spread due to the intrabeam scattering effect as a function of the averaged Twiss beta function and transverse normalized emittance (top) and the Twiss beta function only with 0.1 mm mrad normalized emittance (bottom).

where $\sigma_{\gamma 0}$ is the initial RMS uncorrelated energy spread, r_e is the classical electron radius, N_b is the number of electrons inside the beam, $\ln \Lambda$ is the Coulomb logarithm, $< \sigma_x >$ is the averaged horizontal RMS size, ϵ_x^n is the normalized horizontal emittance, and σ_z is the RMS bunch length. According to the above reference, for a 0.1 mm mrad normalized transverse emittance electron beam, the Coulomb logarithm $\ln \Lambda$ is about 6.0. Assuming a 100 pC charge beam with 100 MeV energy and 1 mm longitudinal RMS bunch length, one obtains the uncorrelated energy spread growth after 36 meters as a function of the averaged Twiss beta function value and the normalized emittance in Fig. 5. The uncorrelated energy spread as a function of the Twiss beta function value with 0.1 mm mard normalized emittance is also shown in the same plot. It is seen that more than 5 keV uncorrelated energy spread can be generated through the intrabeam scattering effect by using a lattice Twiss beta function value below 0.5 meters. For a choice of 0.1 mm mrad normalized emittance and 0.5 meter beta function, it yields 6.6 keV uncorrelated energy spread growth. This level of uncorrelated energy spread can significantly mitigate the microbunching instability gain through the x-ray linear accelerator from the above analytical gain calculation.

In order to generate uncorrelated energy spread through the intrabeam scattering effect in the x-ray linear accelerator, we suggest using a FODO lattice as shown in Fig. 6. Here each period of the lattice consists of a drift of 0.1 meter, a quadrupole of 0.1 meter with a focusing strength $48/m^2$, a drift of 0.2 meter, another quadrupole of 0.1 meter with a focusing strength $-48/m^2$, and another drift of 0.1 meter. Figure 7 shows an electron beam transverse RMS size evo-

Figure 6: Schematic plot of the FODO lattice used to increase the electron beam uncorrelated energy spread.

lution through five periods of the FODO lattice with 0.5 meter averaged Twiss beta function value. The averaged transverse beam size is about 16 microns. The electron beam energy is 100 MeV with 0.1 mm mrad normalized emittance.

The simple model (Eq. 15) in this section suggests that the IBS-induced energy spread should be proportional to the square root of the length of the section and the number of electrons, and inversely proportional to the square root of the average transverse RMS size, beam normalized emittance, and the electron beam RMS bunch length. It does not have an explicit dependence

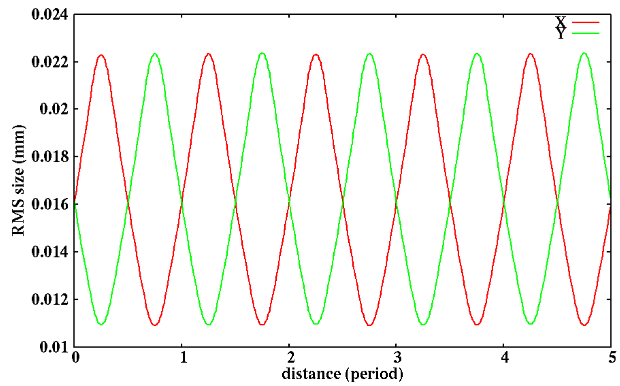

Figure 7: Transverse RMS size evolution through the FODO lattice that helps increase the uncorrelated energy spread.

on the beam energy. In order to attain a larger energy spread, one can use a stronger magnetic focusing to make a smaller transverse beam size, an injector to produce a lower emittance and a short bunch length (higher current) beam, or more electrons and longer distance.

4. Demonstration the feasibility through the X-ray FEL linear accelerator

In order to demonstrate the feasibility of the above suggested method to mitigate the microbunching instability through the accelerator, we solved the Fokker-Planck equation that includes the intrabeam scattering effect self-consistently. The Fokker-Planck equation with the Landau collisional term to account for the scattering effect for a single particle distribution is given as [41]:

$$\frac{\partial f}{\partial t} + \mathbf{v} \cdot \frac{\partial f}{\partial \mathbf{r}} + \frac{\mathbf{F}}{m} \cdot \frac{\partial f}{\partial \mathbf{v}} = -\frac{\partial}{\partial \mathbf{v}} \cdot \mathbf{F}_d f + \frac{1}{2} \frac{\partial^2}{\partial \mathbf{v} \partial \mathbf{v}} : \mathbf{D} f \qquad (16)$$

where $\mathbf{F}_d$ is the dynamic friction vector coefficient and $\mathbf{D}$ is the diffusion matrix coefficient. These coefficients can be obtained from the following equations:

$$\mathbf{F}_d = (\frac{1}{4\pi\epsilon_0})^2 \frac{4\pi e^4}{m^2}\lambda\frac{\partial H}{\partial \mathbf{v}} \quad (17)$$

$$\mathbf{D} = (\frac{1}{4\pi\epsilon_0})^2 \frac{4\pi e^4}{m^2}\lambda\frac{\partial^2 G}{\partial \mathbf{v}\partial \mathbf{v}} \quad (18)$$

where H and G are Rosenbluth potentials [42]:

$$H = 2\int \mathbf{d}^3\mathbf{v}' \frac{f(\mathbf{v}')}{|\mathbf{v}-\mathbf{v}'|} \quad (19)$$

$$G = \int \mathbf{d}^3\mathbf{v}' f(\mathbf{v}')|\mathbf{v}-\mathbf{v}'| \quad (20)$$

and λ is the Coulomb logarithm given as:

$$\lambda = \ln(\frac{b_{max}}{b_{min}}) \quad (21)$$

where the minimum impact parameter $b_{min} = \frac{1}{4\pi\epsilon_0}\frac{e^2}{mv^2}$ is the classical distance of closest approach, the maximum impact parameter $b_{max} = min(\lambda_D, \sigma)$ with $\lambda_D = \sqrt{\epsilon_0 kT/(ne^2)}$, the Debye length, and σ the RMS beam size. The force $\mathbf{F}$ includes both the external and the space-charge forces. The above Fokker-Planck equation can be solved self-consistently using a Langevin approach [43, 44]. At each step, the contribution of the external and space-charge forces in the Fokker-Planck equation can be handled using a particle-in-cell method in the code like IMPACT [45]. The Rosenbluth potentials in Eqs. 19-20 are obtained by computing the convolutions on three-dimensional velocity grid using a FFT based method in the beam frame. The dynamic friction vector and the diffusion matrix are obtained on the grid using a finite-difference approximation to Eqs. 17-18 and then interpolated onto individual particles according to their velocities. The particle velocity due to the intrabeam scattering effect is advanced with the solution of the following equation in the beam frame:

$$\mathbf{v}' = \mathbf{F}_d + \mathbf{\Gamma}(t) \quad (22)$$

where the superscript prime denotes derivative with respect to time, $\mathbf{\Gamma}(t)$ is a vector of random variables that follows a multivariate normal distribution with zero means and covariance matrix $\mathbf{D}$.

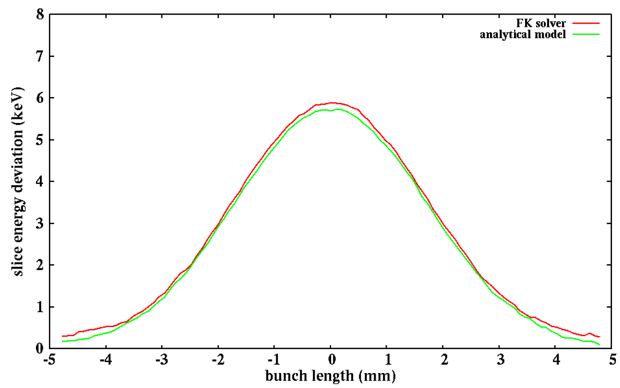

Figure 8: Slice uncorrelated energy spread profile at the exit of the FODO lattice from the self-consistent Fokker-Planck solver (red) and from the analytical model (green).

The above self-consistent solution to the Fokker-Planck equation was benchmarked with a multi-slice analytical model using an initial 6D Gaussian distribution electron beam transporting through the above low beta FODO lattice. The uncorrelated energy spread growth as a function of distance s due to the intrabeam scattering effect from the analytical model is given as [38]:

$$< \Delta\gamma^2 > = 2\pi^{3/2} r_e^2 n_e(x,y,z) \ln\Lambda \frac{1}{\sigma_\beta(z)\gamma_b} s \quad (23)$$

where γ_b is the relativistic factor of the beam, n_e and σ_β are the electron density and the RMS normalized velocity spread. In this model, the local electron density distribution is approximated as a product of a local current and a two-dimensional transverse Gaussian distribution. For a round symmetric beam with a Gaussian current distribution, this model recovers the above Eq. 15 after averaging over all electrons of the beam.

Figure 8 shows the slice uncorrelated energy spread of the electron beam at the exit of FODO lattice from the self-consistent Fokker-Planck solver and from the analytical model. It is seen that both methods agree with each other very well. In this benchmark, we used one million macroparticles to sample the initial Gaussian distribution and $64 \times 64 \times 64$ grid points to compute the Rosenbluth potentials in the Fokker-Planck solver and 50 slices to compute the RMS beam sizes and velocities in the multi-slice analytical model. The Coulomb logarithm is assume as 6.0 for the purpose of benchmark in this example.

As a demonstration, the above low beta FODO lattice was inserted in an LCLS-II-HE alike x-ray FEL linear accelerator as shown in Fig. 1 to generate sufficient uncorrelated energy spread to mitigate the microbunching instability through the accelerator. The LCLS-II-HE linear accelerator is a high energy upgrade of the high repetition rate X-ray FEL, LCLS-II [26, 27], from 4 GeV to 8 GeV and photon spectral range to 12.8 keV with potential to be extended through 20 keV [46]. It consists of a low emittance injector, a laser heater to suppress the microbunching instability, a section of superconducting linac L1, a bunch compressor BC1, a second section of superconducting linac L2, a bunch compressor BC2, a third section of superconducting linac L3 to accelerate the beam to 8 GeV, a long bypass transport line, and a kicker to distribute the electron beam to a soft X-ray transport beam line and to a hard X-ray transport beam line. The superconducting linacs in all three sections are made of 1.3 GHz 9 cell superconducting cavities except the two cryomodules of 3.9 GHz third harmonic cavities right before the BC1 to linearize the electron beam longitudinal phase space. In this study, we replaced the laser heater section with 60 periods of the above 0.5 m beta function FODO lattice and removed the long transport lines. We assumed a dechirper at the end of L3 to remove the longitudinal chirp of the electron beam. Both the three-dimensional space-charge effect and the intrabeam scattering effect were included in the simulation self-consistently. Here, we have used 625 million macroparticles and $64 \times 64 \times 2048$ grid points to compute the Coulomb potential of the space-charge effect and the Rosenbluth potentials of the intrabeam scattering effect in the beam frame.

We started with an initial electron beam distribution at the exit of a modified compact low emittance injector design [33]. This distribution was obtained by running the self-consistent multi-particle tracking simulation with the real number of a 100 pC charge electrons through the low emittance injector using the IMPACT-T code [47]. Using the real number of electrons helps capture the shot noise in the initial electron beam. Figure 9 shows the initial current profile at the entrance to the linear accelerator from the low emittance injector output. The peak current is less than 12 A with 1.0 mm RMS bunch length. The transverse normalized emittance is 0.1 mm mrad. The uncorrelated energy spread is about 1 keV.

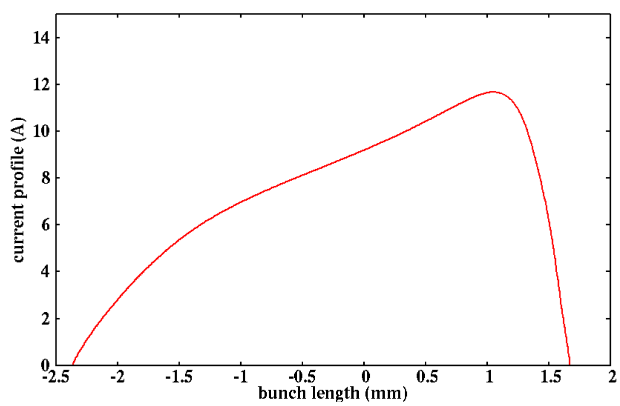

Figure 9: Initial current profile at the entrance of the accelerator.

This initial distribution was matched into the above 60 period low beta

FODO lattice and then rematched into the first linac section (L1) lattice. Figure 10 shows the electron beam transverse RMS size evolution through the entire linear accelerator and through the matching section, the low beta FODO lattice, and L1 linac. It is seen that the initial RMS beam size is less than 200 micron and decreases gradually through the accelerator due to acceleration damping. Inside the low beta FODO lattice, the electron RMS size is squeezed below 20 microns but well-matched through the lattice. Figure 11 shows the transverse RMS projected emittance evolution through the linear accelerator. It is seen that the emittance is reasonably preserved through the accelerator. The major horizontal emittance growth is after BC2 due to the coherent synchrotron radiation effect. The emittance growth through the low beta FODO lattice is small.

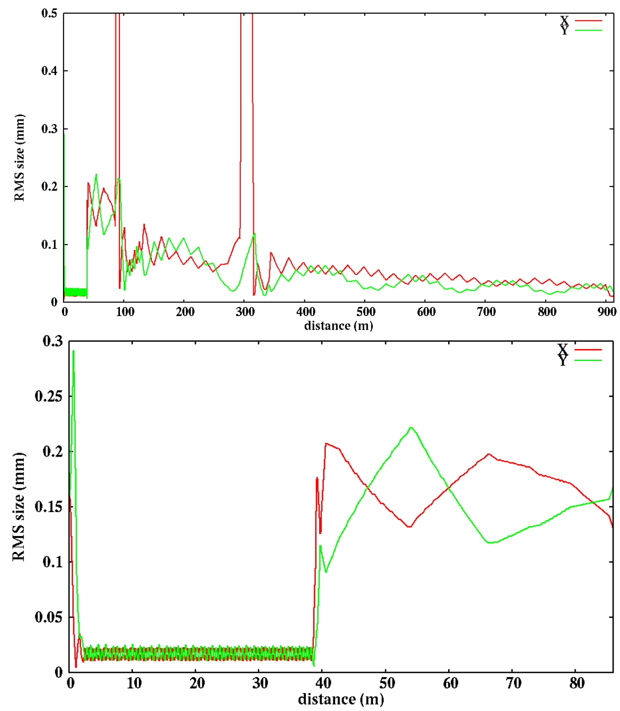

Figure 10: Electron beam RMS size evolution through the entire linear accelerator (top) and through IBS FODO lattice and L1 (bottom).

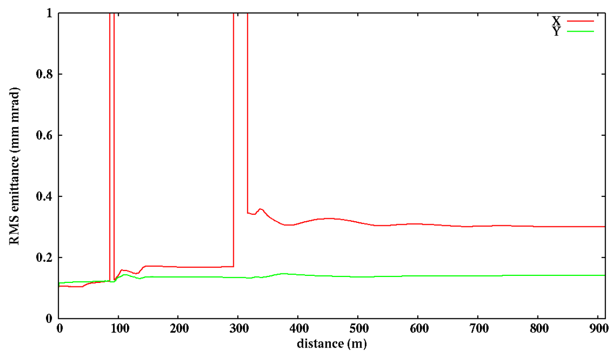

Figure 11: Electron beam RMS emittance evolution through the linear accelerator.

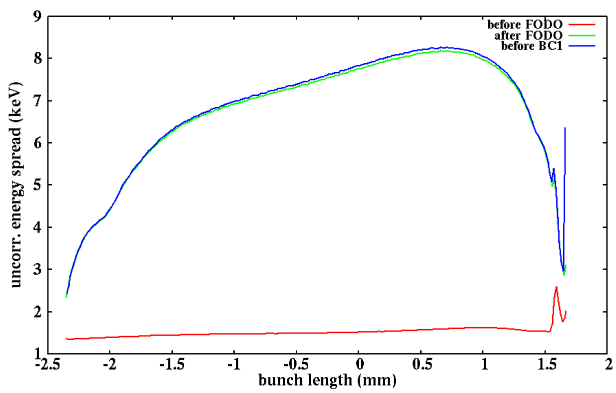

Figure 12: Electron beam slice uncorrelated energy spread before (red), after (blue) the FODO lattice, and before the bunch compressor one (green).

Figure 12 shows the electron beam slice uncorrelated energy profile before, after the low beta FODO lattice, and before the bunch compressor one. It is seen that after the low beta FODO lattice, the electron beam attains near 8 keV uncorrelated energy spread. There is little uncorrelated energy spread growth before the BC1 through the linear accelerator section L1 due to the larger transverse beam size in this section. From the above microbunching instability gain calculation, such a level of uncorrelated energy spread should be able to substantially mitigate the effect of the microbunching instability.

Figure 13 shows the final longitudinal phase space, current profile, uncorrelated energy profile at the exit of the linac three (L3). A dechirper was used to remove the linear correlation in the longitudinal phase space. The effect of the

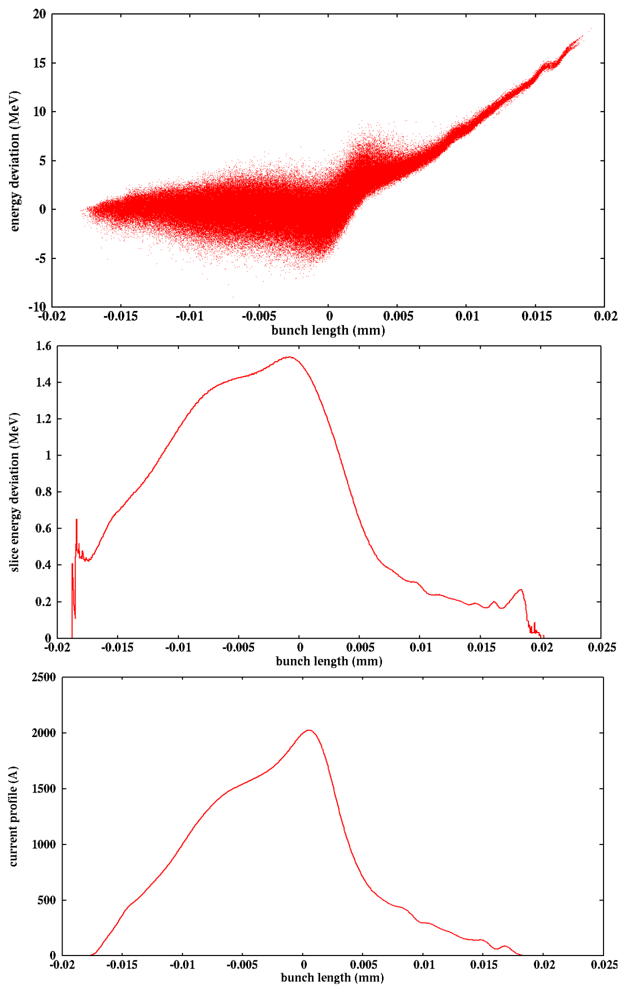

Figure 13: Electron beam final longitudinal phase space (top), uncorrelated energy spread (middle), and current profile (bottom) at the exit of the linear accelerator.

microbunching instability is not noticeable in the longitudinal phase space. The final core peak current is near 2 kA with a maximum uncorrelated energy spread of about 1.5 MeV. Figure 14 shows the final transverse slice emittance at the exit of the linear accelerator. For the flat core longitudinal phase space, both the horizontal and vertical slice emittances are below 0.15 mm mrad. The initial low emittance of the beam is reasonably well preserved through the accelerator.

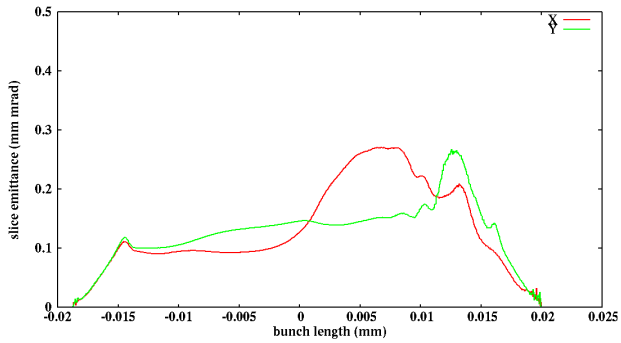

Figure 14: Electron beam final transverse slice emittance at the exit of the linear accelerator.

5. Conclusions

The microbunching instability in an x-ray FEL linear accelerator can cause significant degradation of electron beam brightness and was normally controlled by using a costly laser heater at the entrance of the accelerator. In this paper, we studied the microbunching instability in a different regime of an x-ray FEL linear accelerator with an initial lower peak current high brightness electron beam. In this regime, we observed that modest initial uncorrelated energy spread can substantially reduce the microbunching instability gain. Instead of using the laser heater, we suggested an alternative method that uses a section of low beta FODO lattice to mitigate the microbunching instability for the x-ray FEL linear accelerator with a low emittance injector. Using a 100 pC electron beam with 0.1 mm mrad and 1 mm RMS bunch length, the intrabeam scattering effect through a 36 m low beta FODO lattice induces nearly 8 keV uncorrelated energy spread. Such an uncorrelated energy spread is sufficient to mitigate the microbunching instability gain through a double-chicane linear accelerator. In order to demonstrate the feasibility of the suggested method, we solved the Fokker-Planck equation with Landau collisional term to account for the intrabeam scattering effect self-consistently using the Langevin approach. The self-consistent simulation through an LCLS-II-HE alike x-ray FEL linear accelerator with the low beta FODO lattice instead of the laser heater showed no microbunching instability effect on the final electron longitudinal phase space with a near 2 kA core peak current. The transverse emittance through the low beta FODO lattice and the accelerator was reasonably well preserved in the simulation. This suggests that the low beta FODO lattice method could be used as an effective method to mitigate the microbunching instability in this type of x-ray FEL linear accelerator with a low emittance injector. The suggested FODO lattice in this study might still be too long to fit into any existing x-ray FEL accelerator facilities. It could be useful in the future x-ray FEL accelerator by including this lattice early in the design or by combining this lattice with multiple bending magnets to shorten the straight distance between the entrance and the exit of IBS heating section.

ACKNOWLEDGEMENTS

We would like to thank Drs. F. Ji, C. Mayes, and M. Woodley for some LCLS-II-HE design parameters used in this study and Dr. T. Raubenheimer for bringing the author's attention to the intrabeam scattering effect in LCLS-II-HE design study. This research was supported by the U.S. Department of Energy under Contract No. DE-AC02-05CH11231, and used computer resources at the National Energy Research Scientific Computing Center (NERSC).

References

[1] M. Borland et al., Nucl. Instrum. Methods Phys. Res., Sect. A vol. 483, p. 268, (2002).

[2] E. L. Saldin, E. A. Schneidmiller, and M. V. Yurkov, Nucl. Instrum. Methods Phys. Res., Sect. A, vol. 483, p. 516, (2002).

[3] S. Heifets, G. Stupakov, and S. Krinsky, Phys. Rev. ST Accel. Beams, vol. 5, p. 064401, (2002).

[4] Z. Huang and K. J. Kim, Phys. Rev. ST Accel. Beams, vol. 5, 074401, (2002).

[5] Z. Huang, M. Borland, P. Emma, J. Wu, C. Limborg, G. Stupakov, and J. Welch, Phys. Rev. ST Accel. Beams, vol. 7, 074401, (2004).

[6] M. Venturini, R. Warnock, and A. A. Zholents, Phys. Rev. ST Accel. Beams 10 , 054403, (2007).

[7] R. A. Bosch, K. J. Kleman, and J. Wu, Phys. Rev. ST Accel. Beams 11, 090702, (2008).

[8] J. Wu, Z. Huang, and P. Emma, Phys. Rev. ST Accel. Beams 11, 040701 (2008).

[9] S. Di Mitri, M. Cornacchia, S. Spampinati, and S. Milton, Phys. Rev. ST Accel. Beams 13, 010702 (2010).

[10] S. Seletskiy, B. Podobedov, Y. Shen, and X. Yang, Phys. Rev. Lett. 111, 034803, (2013).

[11] D. Ratner, C. Behrens, Y. Ding, Z. Huang, A. Marinelli, T. Maxwell, and F. Zhou, Phys. Rev. ST Accel. Beams, vol. 18, 030704, (2015).

[12] J. Qiang, Y. Ding, P. Emma, Z. Huang, D. Ratner, T. O. Raubenheimer, F. Zhou, and M. Venturini,Phys. Rev. Accel. Beams 20, 054402 (2017).

[13] E. L. Saldin, E. A. Schneidmiller, and M.V. Yurkov, DESY Report No. TESLA-FEL-2003-02, (2003).

[14] Z. Huang et al., Phys. Rev. ST Accel. Beams 13, 020703 (2010).

[15] P. Emma et al., Nature Photon. 4, 641 (2010).

[16] E. Allaria et al., Nature Photon. 6, 699 (2012).

[17] H. Weise and W. Decking, in Proceedings of the 2017 Free Electron Laser Conference, (JACoW, Geneva, 2017), pp. 9-13.

[18] H.-S. Kang et al., PAL-XFEL technical design report, Pohang Accelerator Laboratory, (2014).

[19] C. Milne et al., SwissFEL: The Swiss x-ray free electron laser, Appl. Sci. 7, 720 (2017).

[20] C. Behrens, Z. Huang, and D. Xiang, Phys. Rev. ST Accel. Beams 15 , 022802 (2012).

[21] J. Qiang, C. E. Mitchell, M. Venturini, Phys. Rev. Lett. 111, 054801, 2013.

[22] S. Di Mitri, S. Spampinati,Phys. Rev. Lett. 112, 134802 (2014).

[23] D. Huang, C. Feng, H. Deng, Q. Gu, and Z. Zhao, Phys. Rev. ST Accel. Beams **19**, 100701 (2016).

[24] T. Liu, W. Qin, D. Wang, and Z. Huang, Phys. Rev. ST Accel. Beams **20**, 082801 (2017).

[25] B. Li and J. Qiang, Phys. Rev. Accel. Beams **23**, 014403 (2020).

[26] T. O. Raubenheimer et al., in Proceedings of the 2015 Free Electron Laser Conference, Daejeon, Korea, (JACoW, Geneva, 2015), pp. 618-624.

[27] LCLS-II Conceptual Design Report, SLAC-R-1092, http://slac.stanford.edu/pubs/slacreports/reports09/slac-r-1092.pdf.

[28] N. Huang, H. Deng, B. Liu, et al., in 39th Free Electron Laser Conf.(FEL'19), Hamburg, Germany, 26-30 August 2019 (JACOW Publishing, Geneva, Switzerland, 2019) pp. 199-202.

[29] S. DiMitri, Phys. Rev. ST Accel. Beams 17, 074401 (2014).

[30] C. E. Mitchell, "Beam dynamics optimization in high-brightness electron injectors," in 9th Int. Particle Accelerator Conf. (IPAC'21), Campinas, Brazil, May 2021, TUXA02.

[31] H. J. Qian, "Review of High Brightness Photoinjectors," in 9th Int. Particle Accelerator Conf. (IPAC'21), Campinas, Brazil, May 2021, TUXX01.

[32] R. R. Robles, O. Camacho, A. Fukasawa, N. Majernik, and J. B. Rosenzweig Phys. Rev. Accel. Beams 24, 063401, (2021).

[33] F. Ji, C. Adolphsen, R. Coy, L. Ge, C.E. Mayes, T.O. Raubenheimer, L. Xiao, J. Qiang, "Beam Dynamics Studies on a Low Emittance Injector for LCLS-II-HE," in Proc. of NAPAC2022, Albuquerque, NM, USA, August, 2022, WEPA02.

[34] E. L. Saldin, E. A. Schneidmiller, and M.V. Yurkov, Nucl. Instrum. Methods Phys. Res. A 528, 355 (2004).

[35] Z. Huang and J. Wu, "Microbunching instability due to bunch compression," in ICFA Beam Dynamics Newsletter, No.38, p. 37, ed. by I. S. Ko, (2005).

[36] J. Qiang, R. D. Ryne, M. Venturini, A. A. Zholents, and I. V. Pogorelov, Phys. Rev. ST Accel. Beams, vol. 12, 100702, (2009).

[37] Z. Huang, "Intrabeam scattering in an x-ray FEL driver," SLAC-TN-05-026, (2002).

[38] G. Penn, “Intra-beam scattering for free electron lasers and its modeling in chicanes,” LBNL report 6762, (2014).

[39] S. DiMitri et al., New J. Phys. 22, 083053, (2020).

[40] C. Tsai, W. Qin, K. Fan, X. Wang, J. Wu, and G. Zhou, Phys. Rev. Accel. Beams, vol. 23, 124401, (2020).

[41] L. Landau, Phys. Z. Sowjetunion (USSR) 10, 154 (1936).

[42] M. N. Rosenbluth, W. M. MacDonald, and D. L. Judd, Phys. Rev. 107, 1 (1957).

[43] H. Risken, The Fokker-Planck Equation: Methods of Solution and Applications, Springer, New York, 1996.

[44] J. Qiang, S. Habib and R. Ryne, “Self-Consistent Langevin Simulation of Coulomb Collisions in Charged-Particle Beams,” Technical Paper, SC2000 (Dallas, November 2000).

[45] J. Qiang, R. D. Ryne, S. Habib, V. Decyk, J. Comput. Phys. **163**, 434, (2000).

[46] T.O. Raubenheimer, “The LCLS-II-HE, A High Energy Upgrade of the LCLS-II”, in Proc. FLS’18, Shanghai, China, Mar. 2018, pp. 6-11. doi:10.18429/JACoW-FLS2018-MOP1WA02.

[47] J. Qiang, S. Lidia, R. D. Ryne, and C. Limborg-Deprey, Phys. Rev. ST Accel. Beams **9**, 044204, (2006).